

Magnet dimensioning in D0FUS: Impact of mechanical configuration

Timothé Auclair¹, Baptiste Boudes¹, Eric Nardon¹, Alexandre Torre¹, Yanick Sarazin¹

¹ CEA, IRFM, F-13108 Saint-Paul-lez-Durance, France

timothe.auclair@cea.fr

Keywords: Magnet design, System code, D0FUS

Abstract

D0FUS is a new toy system code written in Python and designed to enable fast, extensive, and easily interpretable parameter scans. Here, we present its mechanical model, its validation, and the first associated results. These include a comparison of wedging, buckling, and plugged models for central stress resistance, as well as D-shape and C-Clamp for tensile strength.

1 Introduction

The toy model system code D0FUS has the capability to approximate the dimensions of the main thicknesses composing a Tokamak Power Plant (TPP). The most critical thicknesses are those on the high-field side, where space is most constrained. A typical cross-sectional view of an internal leg (radial build) is shown in Fig. 1.

In D0FUS, the first two thicknesses—the plasma radius (a) and the combined thickness of the first wall, breeding blanket, neutron shield, and associated gaps (b)—are inputs to the code. The determination of the toroidal field (TF) coil thickness (c) is described in this chapter, considering several mechanical configurations (e.g., wedging, buckling, C-Clamp). Once the TF thickness is determined, Chapter 3 details the sizing of the central solenoid (CS) performed in D0FUS, which accounts for three mechanical configurations (wedging, buckling, and plugged). Finally, in the case of the plugged configuration, determining the CS thickness (d) includes assessing the required mechanical strength of the central insert.

Two significant issues are neglected here: out-of-plane forces and the need to limit ripple. Both lie outside the 0D/1D framework of our approach.

2 Toroidal field coil model

Starting from the outer radius of the TF coils R_{TF}^{ext} , we will first seek to determine R_{TF}^{int} , the inner radius of the Toroidal Field (TF) coil and the associated TF thickness c . We will aim to meet two criteria: the resistance of mechanical stresses and the generation of the targeted magnetic fields B_{max} .

2.1 Magnetic field generation

To account for the first requirement of carrying enough current to generate B_{max} , we make use of the ampere theorem :

$$B_{max} = \mu_0 J_{Engineering} (R_{TF}^{ext} - R_{TF}^{int}) \quad (1)$$

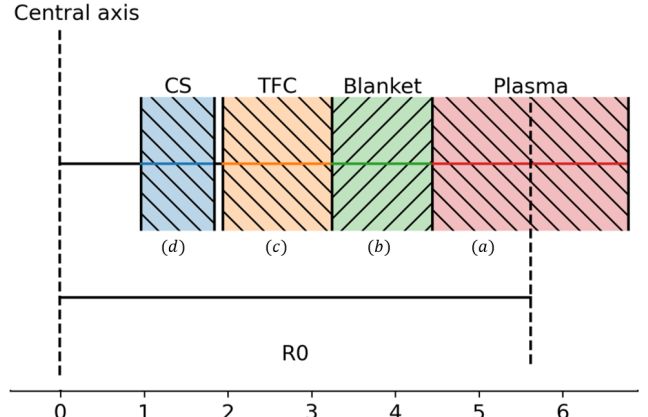


Figure 1: Typical radial build in D0FUS (wedging)

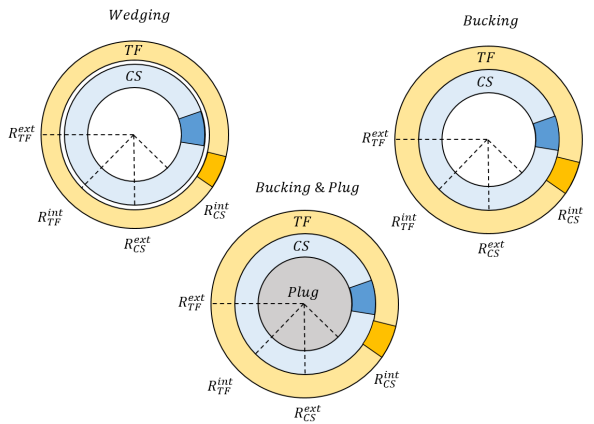


Figure 2: Top view with radius parametrisation in wedging (left), bucking (center) and bucking+plug (right)

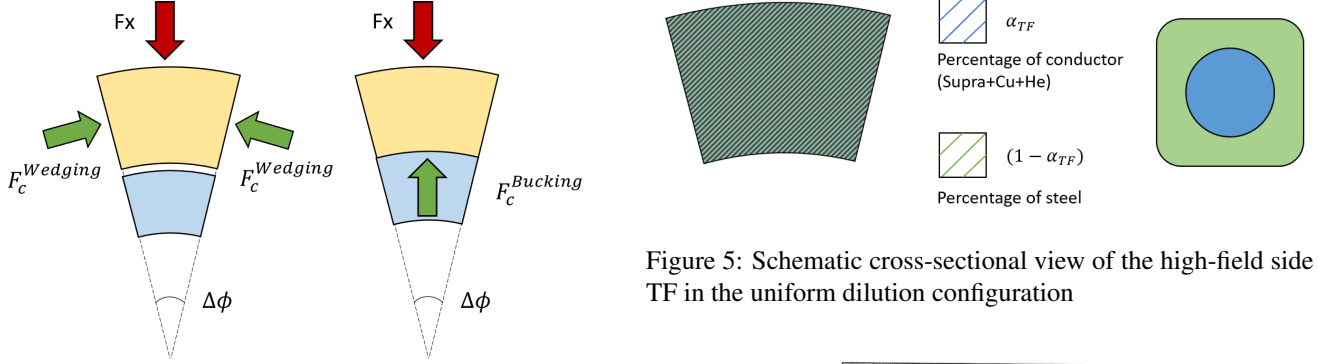


Figure 3: Top view with in plane force in the TF for wedging (left) and bucking (right) configurations

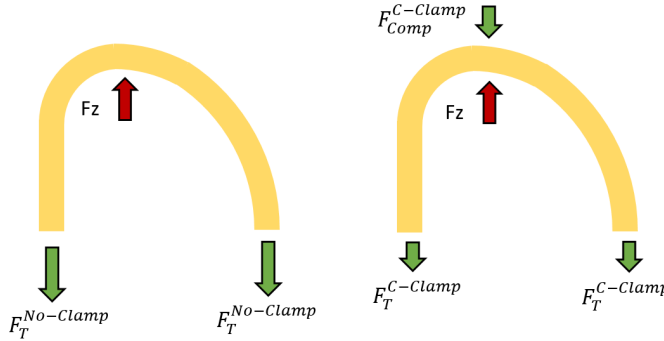


Figure 4: Side view with in plane force for No-Clamp (left) and C-Clamp (right) configurations in the TF

2.2 Mechanical stress

The electromagnetic forces (expansion forces) acting on the TF consist of two components: a centering force along the x-axis and a tensile force along the z-axis. The TF must then be dimensioned to endure the resulting Tresca stress, which combines the tensile stress σ_T from F_z and the centering stress σ_C from F_x .

$$\sigma_{\text{TRESCA}} = \sigma_T + \sigma_C$$

2.2.1 Bucking

The bucking configuration, as shown in Figures 3 and 3, involves supporting the inner leg of the toroidal field (TF) coils on the central solenoid (CS) to transfer the centering forces to it: the TF coils are considered to have no contact between them.

For this configuration, we choose to consider a single isotropic material whose properties are averaged, characterised by a dilution factor representing the distribution between the conductor (superconductor + copper + helium) and steel in its composition. This factor is defined as $\alpha_{\text{TF}} = \frac{V_{\text{conductor}}}{V_{\text{total}}}$ and allows for the expression of $J_{\text{Engineering}} = J_{\text{max}} \alpha_{\text{TF}}$ and $\sigma_{\text{TRESCA}} = \sigma_{\text{max}} (1 - \alpha_{\text{TF}})$ considering a linear decrease of mechanical properties with the percentage of steel.

This approach mimics a coil with uniform repartition of conductor as considered for example in ARIES-RS studies¹ as shown in Fig.6.

The centering force F_x due to the difference of loading between the inner and outer legs (related to the $\frac{1}{r}$ decay of B), can

Figure 5: Schematic cross-sectional view of the high-field side TF in the uniform dilution configuration

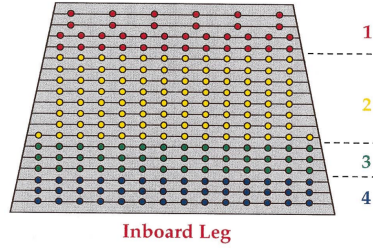


Figure 6: ARIES-RS TF cross-section taken from¹

be expressed as follows (details of this calculation can be found in A):

$$F_x = F_{\text{in}} - F_{\text{out}} =$$

With

$$F_{\text{in}} = \frac{-2h\Delta\phi R_0 B_0^2}{\mu_0} \frac{\left(2 - 2\varepsilon_b - \frac{4\varepsilon_c}{3}\right)}{(2 - 2\varepsilon_b - \varepsilon_c)^2}$$

$$F_{\text{out}} = \frac{-2h\Delta\phi R_0 B_0^2}{\mu_0} \frac{\left(2 + 2\varepsilon_b + \frac{4\varepsilon_c}{3}\right)}{(2 + 2\varepsilon_b + \varepsilon_c)^2}$$

With h defined as the height of the coil, ε_b as $\frac{a+b}{R_0}$ and ε_c as $\frac{c}{R_0}$.

In bucking, we simply have $F_C^{\text{bucking}} = F_x$ as visible in Fig.3 leading to a simple expression for $\sigma_C^{\text{bucking}}$:

$$\sigma_C^{\text{bucking}} = \frac{F_C^{\text{bucking}}}{\Delta\phi R_{\text{TF}}^{\text{int}} h}$$

$$= \frac{2B_0^2 R_0}{\mu_0 R_{\text{TF}}^{\text{int}}} \left((2 - 2\varepsilon_b - \varepsilon_c)^{-1} - (2 + 2\varepsilon_b + \varepsilon_c)^{-1} \right)$$

The tensile force can be shown to be independent of the shape of our coil. Details of the F_z expression in a rectangular coil can be found in the appendix B.

$$F_z = \frac{\pi}{\mu_0} B_0^2 R_0^2 \ln \left(\frac{1 + \varepsilon_b}{1 - \varepsilon_b} \right)$$

We can now express $F_T^{\text{No-Clamp}}$ considering an equal force distribution of the tension in the high and low field leg as shown in Fig.4:

$$F_T^{\text{No-Clamp}} = \frac{F_z}{2}$$

In the C-Clamp configuration, for now, we only consider a fixed $F_{\text{Comp}}^{\text{C-Clamp}}$ force, taken as input of the code (with default

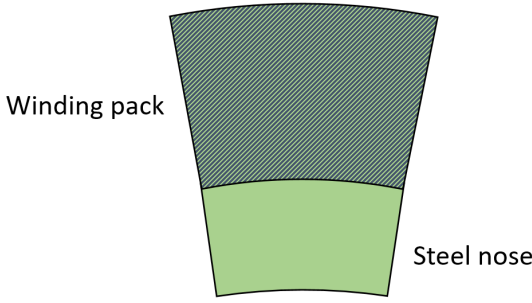


Figure 7: Schematic cross-sectional view of the high-field side TF in the 2 layer configuration

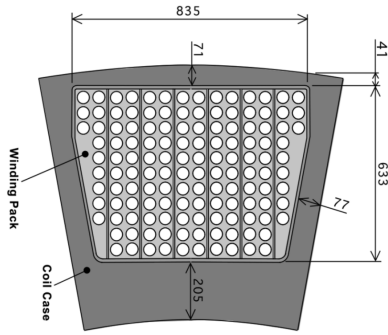


Figure 8: ITER TF cross-section taken from⁷

value of 0N), miming the effect of a C-Clamp providing a pre-compression of the TF. We then can express $F_T^{C-Clamp}$ as:

$$F_T^{C-Clamp} = \frac{F_z - F_{Comp}^{C-Clamp}}{2}$$

Finally, as the surface area is the same between C-Clamp and No-Clamp, one can express the tensile stress σ_T associated to F_T , with F_T beeing $F_T^{C-Clamp}$ or $F_T^{No-Clamp}$:

$$\sigma_T = \frac{F_T}{A_T} = \frac{F_T}{\pi((R_{TF}^{\text{ext}})^2 - (R_{TF}^{\text{int}})^2)}$$

Setting σ_{max} to typical steel value of 660 MPa and J_{max} to a realistic value of 50 MA/m² taken from ITER Nb3Sn allow us to obtain two set of equations with two unknown : c and α_{TF} that can be solved numerically.

2.2.2 Wedging

In the wedging configuration, following Friedberg's approach³, we aim at determining two thicknesses: c_J , the winding pack thickness required to carry the current and transfer the forces, and c_M , the thickness needed to withstand the vault effect due to the contact between TFs as visible in 3

This straightforward approach replicates the design of nose and winding pack approach for TF sizing, typical in wedging, such as those in ITER (Figure 8).

The first thickness, c_J , is determined using the exact same calculations as the TF coil thickness in the bucking configuration, as both must meet the same requirements for current conduction and force transfer.

Afterwards, the nose thickness c_M is dimensionned to withstand the Tresca with the same σ_T than bucking case except the

re-definition of R_{TF}^{ext} to take into account c_J . The major changes concern the centering force that is now demultiplied by a vault effect :

$$F_x = 2F_c^{\text{Wedging}} \sin\left(\frac{\Delta\phi}{2}\right) \approx F_c^{\text{Wedging}} \Delta\phi$$

$$\Rightarrow F_c^{\text{wedging}} \approx \frac{F_x}{\Delta\phi}$$

The centering stress can then be expressed in the wedging case as:

$$\sigma_C^{\text{wedging}} = \frac{F_C^{\text{wedging}}}{2(R_{TF}^{\text{ext}} - R_{TF}^{\text{int}})h}$$

$$= \frac{2B_0^2 R_0}{\mu_0 2(R_{TF}^{\text{ext}} - R_{TF}^{\text{int}})} \left((2 - 2\epsilon_b - \epsilon_c)^{-1} - (2 + 2\epsilon_b + \epsilon_c)^{-1} \right)$$

Since this thickness is composed solely of steel, it can be directly expressed as in Ref.³:

$$c_M = R_0 \left\{ 1 - \epsilon_B - [(1 - \epsilon_B)^2 - \alpha_M]^{1/2} \right\},$$

$$\alpha_M = \frac{B_0^2}{\mu_0 \sigma_{max}} \left[\frac{2\epsilon_B}{1 + \epsilon_B} + \frac{1}{2} \ln \left(\frac{1 + \epsilon_B}{1 - \epsilon_B} \right) \right].$$

3 Central Solenoid derivation

The CS is also treated as a single isotropic material whose properties are averaged over its steel and conductor (including superconductor, copper and cooling) components as in the dilution configuration of the TF. The distribution between steel and conductor is again characterized by a factor $\alpha_{CS} = \frac{V_{\text{conductor}}}{V_{\text{total}}}$, where $V_{\text{conductor}}$ and V_{total} represent respectively the volumes of conductor and total material, as illustrated in Fig. 9.

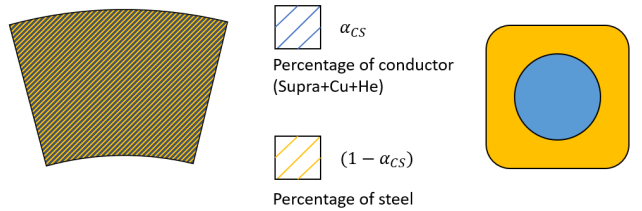


Figure 9: Illustration of the α_{CS} factor definition

3.1 Mechanical criteria

The amount of steel is conservatively calculated to withstand all mechanical stresses without requiring structural support from the conductor. We then define $\sigma_{\text{Engineering}} = \sigma_{CS\text{max}}(1 - \alpha_{CS})$ with $\sigma_{CS\text{max}}$ the mechanical limit of the chosen steel (a typical value is 660 MPa, neglecting fatigue since the machine is supposed to operate in steady-state), and $J_{\text{Engineering}} = J_{CS\text{max}}\alpha_{CS}$ with $J_{CS\text{max}}$ the maximum current density allowed by the chosen conductor (a typical value is 50 MA/m², taken from ITER 3Niobium-Tin cable, neglecting the effect of B on J).

A temporal analysis of the forces acting on the central solenoid (CS) is necessary to identify the limiting cases for sizing the CS. To begin, a schematic (Figure 11) illustrates the

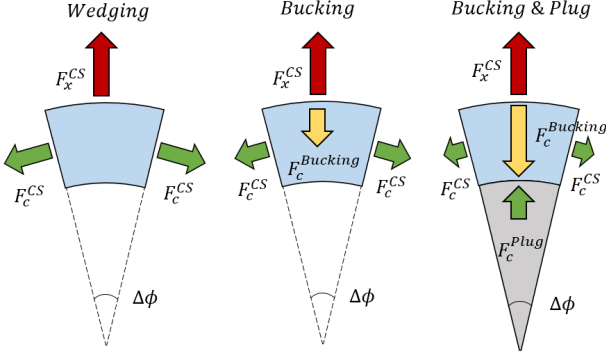


Figure 10: Top view with in plane force in the CS for different mechanical configurations

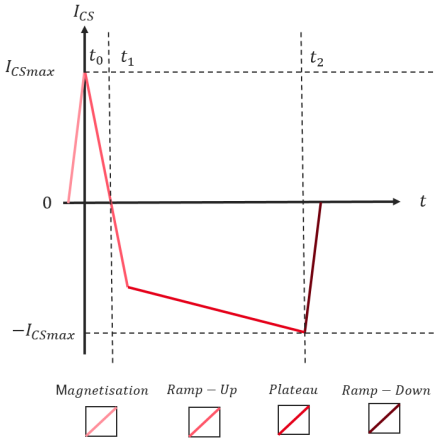


Figure 11: Schematic temporal evolution of the CS current during a discharge

typical evolution of the current in the CS, regardless of the mechanical strategy employed.

The cycle begins with a pre-magnetization phase where the central solenoid current increases to I_{CSmax} , followed by its discharge to ramp up the plasma. During this phase, the current passes through zero at t_1 before reversing, enabling further ramp-up and then, during the plateau, the generation of I_p in the plasma. This example, based on a scenario without current drive (CD), leads to the same mechanical conclusions as steady-state operation. Finally, the current decreases back to $I_{CS} = 0$ during the ramp-down phase.

Three load-bearing configurations are possible for the central solenoid (CS):

3.1.1 Wedging

This configuration relies on an arch effect, where the CS alone withstands its expansion forces. As presented in Figure 12, the critical moments when the CS experiences the highest stress occur at t_0 or t_2 , when the CS reaches $\pm I_{CSmax}$.

We consider a conservative mechanical criterion, as we position ourselves at the inner radius of the CS R_{CS}^{int} , where the magnetic field is maximal, and assume no transfer of stress to other CS layers. The projected stress generated by the $J \times B$ force held through a vault effect can then be expressed as:

$$\sigma_{CSmax} = J_{Engineering} B_{CS} R_{CS}^{int} \quad (2)$$

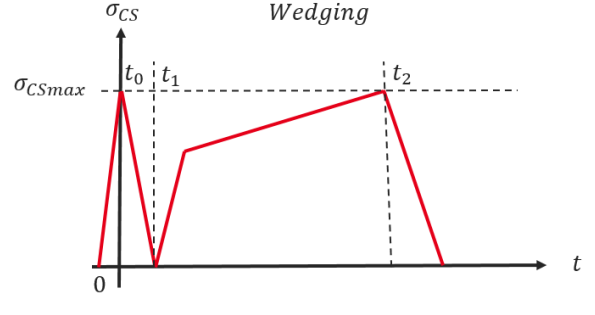


Figure 12: CS stress evolution during a typical discharge in wedging

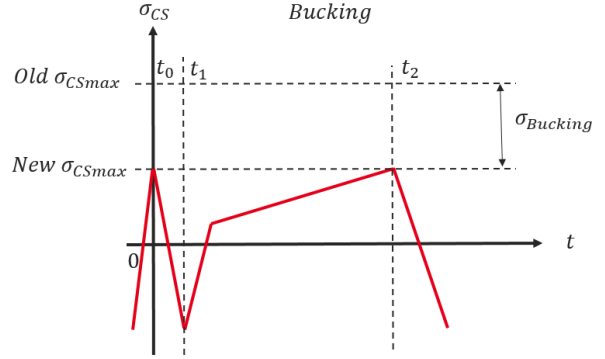


Figure 13: CS stress evolution during a typical discharge in "light" bucking

3.1.2 Bucking

In this configuration, the toroidal field coils transfer their centering force to the CS, resulting in its pre-compression as presented in Fig. 13.

We will seek to determine the stress induced by the transmission of the centering force in the case of bucking. The calculation is equivalent to the force sustained by the vault effect in the TF coils during wedging, but using the radii of the CS :

$$\sigma_{Buckling} = \frac{F_c}{A_{CS}} = \frac{F_c}{(R_{TF}^{int} - R_{CS}^{int}) \cdot h}$$

$$\text{Knowing : } F_x = 2F_c \sin\left(\frac{\Delta\phi}{2}\right) \approx F_c \Delta\phi$$

$$\text{And : } F_c = \frac{2B_0^2 h R_0}{\mu_0} \left((2 - 2\epsilon_b - \epsilon_c)^{-1} - (2 + 2\epsilon_b + \epsilon_c)^{-1} \right)$$

$$\sigma_{Buckling} = \frac{2B_0^2 R_0}{(R_{TF}^{int} - R_{CS}^{int}) \mu_0} \left((2 - 2\epsilon_b - \epsilon_c)^{-1} - (2 + 2\epsilon_b + \epsilon_c)^{-1} \right)$$

We can observe that the most constraining case depends on whether $\sigma_{buckling}$ exceeds σ_{CS} or not, as shown in Figures 13 and 14 with critical time being respectively t_0 and t_2 as in wedging case, or t_1 (representing the most typical case in bucking configuration).

We can then express σ_{CSmax} as:

$$\sigma_{CSmax} = \max(\sigma_{J \times B} - \sigma_{centering}, \sigma_{centering})$$

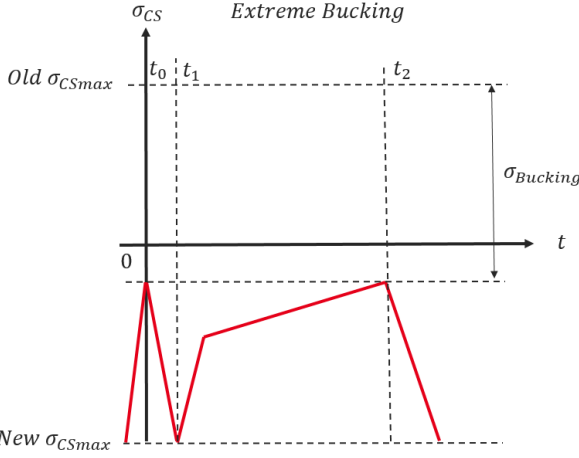


Figure 14: CS stress evolution during a typical discharge in "strong" bucking

3.1.3 Bucking & plug

The addition of a central plug becomes an interesting option when the centering force from bucking exceeds the CS's expansion force (previously called "strong" bucking).

Modèle à développer, attention au possible décollement du CS du à la force d'expansion

3.2 Flux consumption criteria

The magnetic flux requirement, not considering any current drive assistance during the ramp up, is expressed as:

$$\Psi_{\text{Init}} + \Psi_{\text{Ramp-Up}} + \Psi_{\text{Plateau}} = 2\Psi_{\text{CS}} + \Psi_{\text{PF}} \quad (3)$$

In Eq. 3:

- The flux consumption at plasma initiation is difficult to predict. In this paper we chose a probably conservative value: $\Psi_{\text{Init}} = 20 \text{ Wb}$.
- The flux consumption to ramp up the plasma current is composed of two terms, respectively linked to the inductance and the resistance of the plasma:

$$\begin{aligned} \Psi_{\text{Ramp-Up}} &= \Psi_{\text{Ind}} + \Psi_{\text{Res}} = L_p I_p + C_{\text{Ejima}} \mu_0 R_0 I_p \\ &= \mu_0 R_0 I_p \left(C_{\text{Ejima}} + \frac{l_i}{2} + \log \frac{8R_0}{a\sqrt{\kappa}} - 2 \right) \end{aligned} \quad (4)$$

with the value of the normalized internal inductance l_i fixed by the user (0.5-0.9) or estimated using more refined models^{4,6} and the Ejima constant C_{Ejima} fixed to a standard value of 0.45^{2,8}.

- As the plasma current is assumed to be entirely non-inductively driven, Ψ_{Plateau} is taken equal to 0.
- The CS flux can be expressed as (details of the calculation in appendix C):

$$\Psi_{\text{CS}} = \frac{\pi B_{\text{CS}}}{3} ((R_{\text{CS}}^{\text{ext}})^2 + R_{\text{CS}}^{\text{ext}} R_{\text{CS}}^{\text{int}} + (R_{\text{CS}}^{\text{int}})^2) \quad (5)$$

- The contribution of the PF coils is approximated by calculating the vertical magnetic field and the corresponding flux as in²:

$$B_{\text{vert}} = \frac{\mu_0 I_p}{4\pi R_0} \left(\beta_p + \frac{l_i - 3}{2} + \log \frac{8R_0}{a\sqrt{\kappa}} \right)$$

$$\Psi_{\text{PF}} = B_{\text{vert}} \pi (R_0^2 - (R_{\text{CS}}^{\text{ext}})^2) \quad (6)$$

with β_p approximated from⁵, k_B the Boltzmann constant and L the length of the last closed flux surface:

$$\beta_p = \frac{4\bar{n}k_B T L^2}{\mu_0 I_p^2}$$

We do not consider any contribution of B_{vert} within the CS (this explains the $R_0^2 - (R_{\text{CS}}^{\text{ext}})^2$ factor). Indeed, the CS will be sized to generate a maximum magnetic field that cannot be exceeded, including B_{vert} .

3.3 CS solution

Finally, making use of Ampère's theorem, one can link the magnetic field inside the CS with its radius:

$$B_{\text{CS}} = \mu_0 J_{\text{Engineering}} (R_{\text{CS}}^{\text{ext}} - R_{\text{CS}}^{\text{int}})$$

Ensuring that only solutions satisfying $B_{\text{CS}} < B_{\text{max}}$ are selected, we then obtain a system of two equations with two unknowns (α_{CS} and $R_{\text{CS}}^{\text{int}}$), which can be solved numerically to determine the internal radius of the CS and the optimal distribution between conductor and steel.

4 Benchmark

5 First results

5.1 Central stress recovery

To compare the three possible configurations for recovering centering forces (wedging, bucking, and plug), we performed a parametric scan using the D0FUS system code. This scan explores variations in R_0 and a , while keeping other key parameters fixed: $P_{\text{fus}} = 2 \text{ GW}$, $B_{\text{max}} = 12 \text{ T}$ (representative of Low Temperature Superconductors) in 15 and 20T (representative of High Temperature Superconductors) in 16, $\kappa = 2.1$, $\delta = 0.33$, and $b = 1.2 \text{ m}$. The confinement scaling law used is IPB98(y,2) with $H_{98} = 1$.

Overall, we observe that bucking allows access to a range of solutions with smaller R_0 , which are not accessible with wedging (highlighted in purple in both figures).

This gain in radial build with bucking is explained by the logical reduction in the thickness of the TF coils. In this configuration, the centering force only needs to be transmitted and is no longer amplified by the arch effect between the coils.

On the other hand, the CS thickness remains largely unaffected, as it is always sized to withstand its explosion forces.

Thus, the choice of mechanical configuration depends on the other parameters selected for the machine (e.g., elongation, superconducting technology, etc.). Specifically, and as an example, within the framework of designing a tokamak power plant with $Q > 50$:

- In the 12 T case 15, $Q > 50$ solutions are already accessible with wedging, making bucking unnecessary. - Conversely,

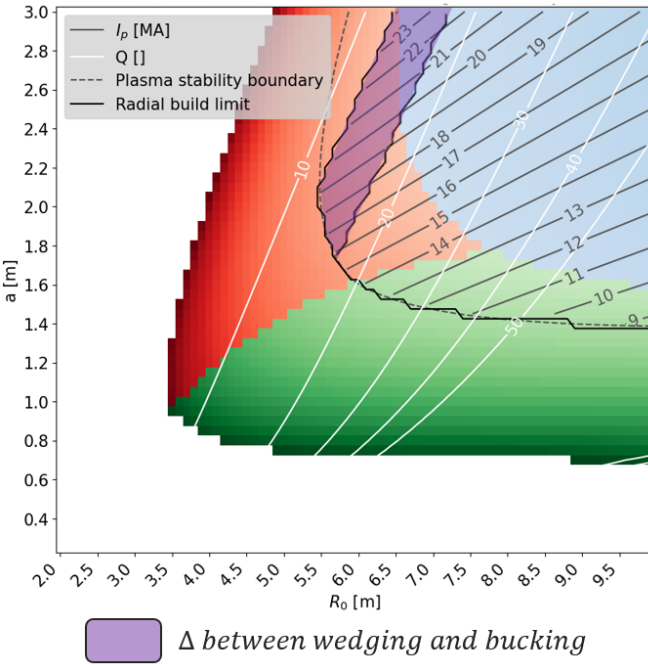


Figure 15: a and R_0 scan with $P_{fus} = 2$ GW and $B_{max} = 12$ T

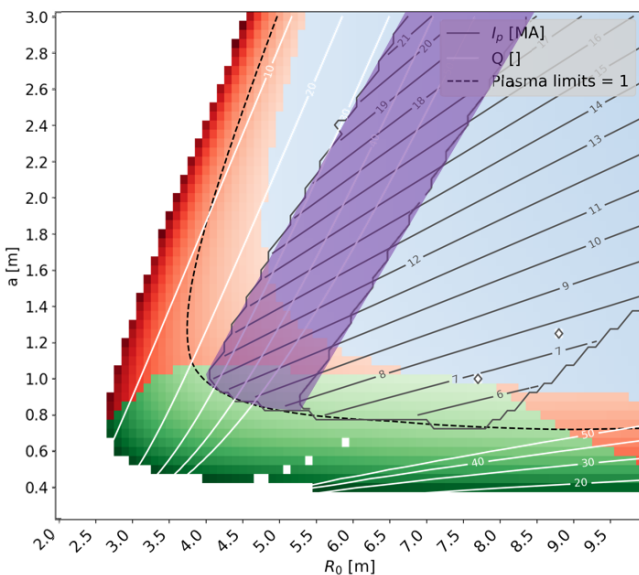


Figure 16: a and R_0 scan with $P_{fus} = 2$ GW and $B_{max} = 20$ T

in the 20 T case 16, bucking demonstrates its advantage by enabling a reduction in the size of the TPP, granting access to a region where the radial build was the limiting factor under wedging.

5.2 Hoop stress recovery

Similarly, to compare the hoop configurations, we perform the same type of scan for different vertical configurations (C-clamp vs. No-clamp).

5.3 Ratio between hoop and centering stress

To investigate the significance of force recovery strategies within the solution space, we aim to study the ratio of stresses due to centering vs hoop forces. Indeed, the importance of using one strategy over another is dictated by this percentage. As an example, if the centering force is predominant, we would logically be more interested in adopting a strategy to manage it rather than focusing on the hoop force.

For now, we focus on the TF, in the wedging case:

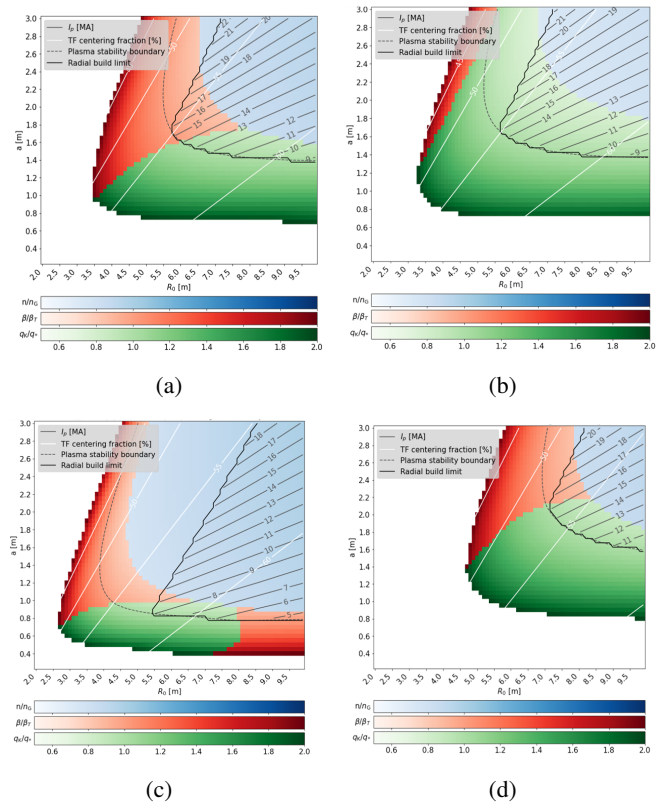


Figure 17: Scan over a and R_0 with the ratio between centering stress and Tresca stress displayed along the white contours

Figure 17a is the equivalent of the reference figure 15, but with the ratio between centering stress and Tresca stress displayed along the white contours.

We can observe that they are not affected by a change in magnetic field ($B_{max} = 20$ T in figure 17c) or fusion power ($P_{fus} = 1.5$ GW in figure 17b).

This can be understood by attempting to analytically express this ratio (details of the calculation in Appendix D):

$$\frac{\sigma_C^{\text{wedging}}}{\sigma_T + \sigma_C^{\text{wedging}}} = \frac{(R_{\text{TF}}^{\text{ext}} + R_{\text{TF}}^{\text{int}}) \left(\frac{1}{2-2\frac{a+b}{R_0}-\frac{c}{R_0}} - \frac{1}{2+2\frac{a+b}{R_0}+\frac{c}{R_0}} \right)}{(R_{\text{TF}}^{\text{ext}} + R_{\text{TF}}^{\text{int}}) \left(\frac{1}{2-2\frac{a+b}{R_0}-\frac{c}{R_0}} - \frac{1}{2+2\frac{a+b}{R_0}+\frac{c}{R_0}} \right) + R_0 \ln \left(\frac{1+\frac{a+b}{R_0}}{1-\frac{a+b}{R_0}} \right)}$$

We observe that, indeed, this ratio depends only on the geometric parameters of the machine, which can be illustrated, for example, with a variation of b (Figure 17d) which indeed allows us to see a variation in the white lines.

However, this study does not highlight solution spaces where the recovery of centering or tensile forces would be significantly more important than others, since in classical geometries, this ratio remains very close to 50%.

Acknowledgements

This work is financially supported by the French government's "France 2030" initiative through the "ANR" (National Research Agency) in the framework of the SupraFusion PEPR Program and its SF-Plant research project.

A Centering force in the TF

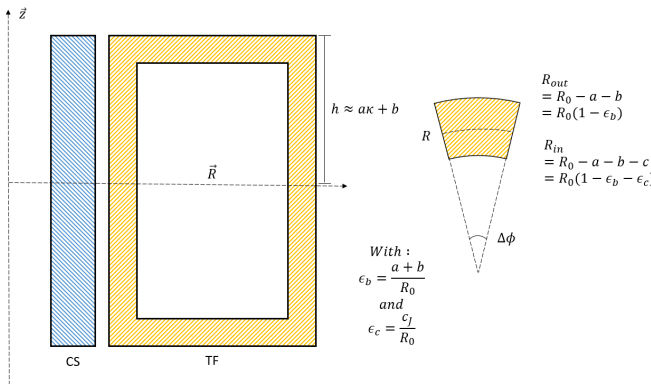


Figure 18: Parameterization for TF calculus

Preliminary calculations using Ampère's theorem:

$$\oint_{\partial S} \mathbf{B} \cdot d\mathbf{l} = \mu_0 I_{\text{enclosed}}$$

1. In the coil to relate B to R :

$$\begin{aligned} I_{\text{enclosed}} &= j\pi(R^2 - R_{\text{in}}^2) \\ \Rightarrow 2\pi RB(R) &= \mu_0 j\pi(R^2 - R_0^2(1 - \varepsilon_b - \varepsilon_c)^2) \\ \Rightarrow B(R) &= \frac{\mu_0 j}{2} \frac{R^2 - R_0^2(1 - \varepsilon_b - \varepsilon_c)^2}{R} \end{aligned}$$

2. At the center of the plasma to relate j to B_0 :

$$I_{\text{enclosed}} = j\pi(R_{\text{out}}^2 - R_{\text{in}}^2)$$

$$\Rightarrow 2\pi R_0 B_0 = \mu_0 j\pi(R_0^2(1 - \varepsilon_b)^2 - R_0^2(1 - \varepsilon_b - \varepsilon_c)^2)$$

$$\Rightarrow j = \frac{2B_0}{\mu_0 R_0 \varepsilon_c (2 - 2\varepsilon_b - \varepsilon_c)}$$

Calculation of the force in the inner leg (F_{In}):

$$F_{\text{in}} = \int_{R_{\text{in}}}^{R_{\text{out}}} \int_0^{\Delta\phi} \int_{-h}^h R(\vec{j} \times \vec{B}) dR d\phi dz$$

$$= -2h\Delta\phi j \int_{R_0(1-\varepsilon_b-\varepsilon_c)}^{R_0(1-\varepsilon_b)} RB(R) dR$$

By replacing with the expression of $B(R)$:

$$= -h\Delta\phi j^2 \mu_0 \int_{R_0(1-\varepsilon_b-\varepsilon_c)}^{R_0(1-\varepsilon_b)} R^2 - R_0^2(1 - \varepsilon_b - \varepsilon_c)^2 dR$$

$$= -h\Delta\phi j^2 \mu_0 \left[\frac{R^3}{3} - RR_0^2(1 - \varepsilon_b - \varepsilon_c)^2 \right]_{R_0(1-\varepsilon_b-\varepsilon_c)}^{R_0(1-\varepsilon_b)}$$

$$= -h\Delta\phi j^2 \mu_0 \left[\frac{R_0^3(1 - \varepsilon_b)^3}{3} - \frac{R_0^3(1 - \varepsilon_b - \varepsilon_c)^3}{3} - R_0^3 \varepsilon_c (1 - \varepsilon_b - \varepsilon_c)^2 \right]$$

$$= -h\Delta\phi j^2 \mu_0 R_0^3 \varepsilon_c^2 \left(1 - \varepsilon_b - \frac{2\varepsilon_c}{3} \right)$$

By reinserting the expression of j^2 :

$$= \frac{-4h\Delta\phi \mu_0 R_0^3 \varepsilon_c^2 B_0^2 \left(1 - \varepsilon_b - \frac{2\varepsilon_c}{3} \right)}{\mu_0^2 R_0^2 \varepsilon_c^2 (2 - 2\varepsilon_b - \varepsilon_c)^2}$$

$$= \frac{-2h\Delta\phi R_0 B_0^2 \left(2 - 2\varepsilon_b - \frac{4\varepsilon_c}{3} \right)}{\mu_0 (2 - 2\varepsilon_b - \varepsilon_c)^2}$$

$$\approx \frac{-2h\Delta\phi R_0 B_0^2}{\mu_0 (2 - 2\varepsilon_b - \varepsilon_c)}$$

B Tensile force in the TF

Reprendre calculs effectués suite à la note de Yanick

C Ψ_{CS} expression

To determine the magnetic flux provided by our CS, we integrate the magnetic field over the transversal cross-section, considering an infinitely large solenoid and a uniformly distributed current density.

$$\begin{aligned}
\Psi_{CS} &= \iint B dS \\
&= 2\pi \left(\int_0^{R_{CS}^{\text{int}}} B_{CS} r dr + \int_{R_{CS}^{\text{int}}}^{R_{CS}^{\text{ext}}} B_{CS} \left(\frac{R_{CS}^{\text{ext}} - r}{R_{CS}^{\text{ext}} - R_{CS}^{\text{int}}} \right) r dr \right) \\
&= 2\pi B_{CS} \left(\frac{(R_{CS}^{\text{int}})^2}{2} + \frac{1}{R_{CS}^{\text{ext}} - R_{CS}^{\text{int}}} \int_{R_{CS}^{\text{int}}}^{R_{CS}^{\text{ext}}} R_{CS}^{\text{ext}} - r dr \right) \\
&= 2\pi B_{CS} \left(\frac{(R_{CS}^{\text{int}})^2}{2} + \frac{1}{R_{CS}^{\text{ext}} - R_{CS}^{\text{int}}} \left(\frac{R_{CS}^{\text{ext}}}{2} ((R_{CS}^{\text{ext}})^2 - (R_{CS}^{\text{int}})^2) \right. \right. \\
&\quad \left. \left. - \frac{1}{3} ((R_{CS}^{\text{ext}})^3 - (R_{CS}^{\text{int}})^3) \right) \right) \\
&= \frac{\pi B_{CS}}{R_{CS}^{\text{ext}} - R_{CS}^{\text{int}}} ((R_{CS}^{\text{int}})^2 (R_{CS}^{\text{ext}} - R_{CS}^{\text{int}}) + (R_{CS}^{\text{ext}})^3 - (R_{CS}^{\text{int}})^2 R_{CS}^{\text{ext}} \\
&\quad - \frac{2}{3} ((R_{CS}^{\text{ext}})^3 - (R_{CS}^{\text{int}})^3)) \\
&= \frac{\pi B_{CS}}{R_{CS}^{\text{ext}} - R_{CS}^{\text{int}}} \left((R_{CS}^{\text{ext}})^3 - (R_{CS}^{\text{int}})^3 - \frac{2}{3} ((R_{CS}^{\text{ext}})^3 - (R_{CS}^{\text{int}})^3) \right) \\
&= \frac{\pi B_{CS}}{3} \left(\frac{(R_{CS}^{\text{ext}})^3 - (R_{CS}^{\text{int}})^3}{R_{CS}^{\text{ext}} - R_{CS}^{\text{int}}} \right) \\
&= \frac{\pi B_{CS}}{3} ((R_{CS}^{\text{ext}})^2 + R_{CS}^{\text{ext}} R_{CS}^{\text{int}} + (R_{CS}^{\text{int}})^2)
\end{aligned} \tag{7}$$

The first term corresponds to the integration over the space between $R = 0$ and $R = R_{CSi}$ (where $B = B_{CS}$), while the second term represents the space within the central solenoid, where, due to our assumption of uniformly distributed current, we consider a linear evolution (see Figure 1). To obtain the total contribution of the central solenoid, this flux value must be multiplied by two. Indeed, the CS has the specificity of achieving a complete inversion of its magnetic field (starting from B_{CS} and ending at $-B_{CS}$) leading to $\Psi_{C\text{total}} = 2\Psi_{CS}$.

D Wedging TF centering ratio

We aim to understand and analyze the dependence of:

$$\begin{aligned}
\frac{\sigma_C^{\text{wedging}}}{\sigma_T + \sigma_C^{\text{wedging}}} &= \frac{1}{1 + \frac{\sigma_T}{\sigma_C^{\text{wedging}}}} \\
\frac{\sigma_T}{\sigma_C^{\text{wedging}}} &= \frac{\frac{1}{2\mu_0((R_{TF}^{\text{ext}})^2 - (R_{TF}^{\text{int}})^2)} B_0^2 R_0^2 \ln \left(\frac{1 + \frac{a+b}{R_0}}{1 - \frac{a+b}{R_0}} \right)}{\frac{2B_0^2 R_0}{\mu_0 2(R_{TF}^{\text{ext}} - R_{TF}^{\text{int}})} \left(\left(2 - 2 \frac{a+b}{R_0} - \frac{R_{TF}^{\text{ext}} - R_{TF}^{\text{int}}}{R_0} \right)^{-1} - \left(2 + 2 \frac{a+b}{R_0} + \frac{R_{TF}^{\text{ext}} - R_{TF}^{\text{int}}}{R_0} \right)^{-1} \right)} \\
&\rightarrow \frac{\sigma_T}{\sigma_C^{\text{wedging}}} = \frac{\frac{R_0}{((R_{TF}^{\text{ext}})^2 - (R_{TF}^{\text{int}})^2)} \ln \left(\frac{1 + \frac{a+b}{R_0}}{1 - \frac{a+b}{R_0}} \right)}{\frac{1}{(R_{TF}^{\text{ext}} - R_{TF}^{\text{int}})} \left(\left(2 - 2 \frac{a+b}{R_0} - \frac{R_{TF}^{\text{ext}} - R_{TF}^{\text{int}}}{R_0} \right)^{-1} - \left(2 + 2 \frac{a+b}{R_0} + \frac{R_{TF}^{\text{ext}} - R_{TF}^{\text{int}}}{R_0} \right)^{-1} \right)}
\end{aligned}$$

Knowing :

$$(R_{TF}^{\text{ext}})^2 - (R_{TF}^{\text{int}})^2 = (R_{TF}^{\text{ext}} - R_{TF}^{\text{int}})(R_{TF}^{\text{ext}} + R_{TF}^{\text{int}})$$

The denominator of σ_T can be rewritten as:

$$\begin{aligned}
\frac{1}{(R_{TF}^{\text{ext}})^2 - (R_{TF}^{\text{int}})^2} &= \frac{1}{(R_{TF}^{\text{ext}} - R_{TF}^{\text{int}})(R_{TF}^{\text{ext}} + R_{TF}^{\text{int}})} \\
\rightarrow \frac{\sigma_T}{\sigma_C^{\text{wedging}}} &= \frac{R_0 \ln \left(\frac{1 + \frac{a+b}{R_0}}{1 - \frac{a+b}{R_0}} \right)}{(R_{TF}^{\text{ext}} + R_{TF}^{\text{int}}) \left(\left(2 - 2 \frac{a+b}{R_0} - \frac{R_{TF}^{\text{ext}} - R_{TF}^{\text{int}}}{R_0} \right)^{-1} - \left(2 + 2 \frac{a+b}{R_0} + \frac{R_{TF}^{\text{ext}} - R_{TF}^{\text{int}}}{R_0} \right)^{-1} \right)} \\
\rightarrow \frac{\sigma_C^{\text{wedging}}}{\sigma_T + \sigma_C^{\text{wedging}}} &= \frac{(R_{TF}^{\text{ext}} + R_{TF}^{\text{int}}) \left(\frac{1}{2 - 2 \frac{a+b}{R_0} - \frac{R_{TF}^{\text{ext}} - R_{TF}^{\text{int}}}{R_0}} - \frac{1}{2 + 2 \frac{a+b}{R_0} + \frac{R_{TF}^{\text{ext}} - R_{TF}^{\text{int}}}{R_0}} \right)}{(R_{TF}^{\text{ext}} + R_{TF}^{\text{int}}) \left(\frac{1}{2 - 2 \frac{a+b}{R_0} - \frac{R_{TF}^{\text{ext}} - R_{TF}^{\text{int}}}{R_0}} - \frac{1}{2 + 2 \frac{a+b}{R_0} + \frac{R_{TF}^{\text{ext}} - R_{TF}^{\text{int}}}{R_0}} \right) + R_0 \ln \left(\frac{1 + \frac{a+b}{R_0}}{1 - \frac{a+b}{R_0}} \right)}
\end{aligned}$$

References

- [1] L Bromberg, P Titus, JS Schultz, M Sidorov, S Pourrahimi, ARIES Team, et al. Aries-rs magnet systems. *Fusion engineering and design*, 38(1-2):159–188, 1997.
- [2] J-L Duchateau, P Hertout, B Saoutic, J-F Artaud, L Zani, and C Reux. Conceptual integrated approach for the magnet system of a tokamak reactor. *Fusion Engineering and Design*, 89(11):2606–2620, 2014.
- [3] JP Freidberg, FJ Mangiarotti, and J Minervini. Designing a tokamak fusion reactor—how does plasma physics fit in? *Physics of Plasmas*, 22(7), 2015.
- [4] GL Jackson, TA Casper, TC Luce, DA Humphreys, JR Ferron, AW Hyatt, Edward Alan Lazarus, RA Moyer, TW Petrie, DL Rudakov, et al. Iter startup studies in the diii-d tokamak. *Nuclear Fusion*, 48(12):125002, 2008.
- [5] Johner Jean. Helios: a zero-dimensional tool for next step and reactor studies. *Fusion Science and Technology*, 59(2):308–349, 2011.
- [6] A Salar Elahi and M Ghoranneviss. Determination of the plasma internal inductance and evaluation of its effects on plasma horizontal displacement in ir-t1 tokamak. *Journal of fusion energy*, 29:76–82, 2010.
- [7] C Sborchia, Y Fu, R Gallix, C Jong, J Knaster, and N Mitchell. Design and specifications of the iter tf coils. *IEEE transactions on applied superconductivity*, 18(2):463–466, 2008.
- [8] RD Stambaugh, VS Chan, AM Garofalo, M Sawan, DA Humphreys, LL Lao, JA Leuer, TW Petrie, R Prater, PB Snyder, et al. Fusion nuclear science facility candidates. *Fusion Science and Technology*, 59(2):279–307, 2011.
- [9] John Wesson and David J Campbell. *Tokamaks*, volume 149. Oxford university press, 2011.